

Optimization of the TES-Bias Circuit for a Multiplexed Microcalorimeter Array

W.B. Doriese · B.K. Alpert · J.W. Fowler · G.C. Hilton · A.S. Hojem ·
K.D. Irwin · C.D. Reintsema · D.R. Schmidt · G.M. Stiehl · D.S. Swetz ·
J.N. Ullom · L.R. Vale

Received: 9 September 2011 / Accepted: 8 January 2012 / Published online: 27 January 2012
© Springer Science+Business Media, LLC (outside the USA) 2012

Abstract A transition-edge-sensor (TES) microcalorimeter's shunt resistor (R_{sh}) and thermal conductance to the cryogenic bath (G) are often considered to be interchangeable knobs with which to control detector speed. Indeed, for otherwise-identical TES-parameter models, there are many combinations of R_{sh} and G that give the same decay time-constant (τ_{crit}). However, our previous work showed that with time- or code-division-multiplexed readout, the distribution of signal-to-noise ratio with frequency, which depends strongly on R_{sh} and G , is just as important as τ_{crit} . Here, we present a set of calculations to select the optimal values of R_{sh} and G , given a linear TES model and count-rate and energy-resolution requirements. Lower G and lower R_{sh} make multiplexing easier. Our calculations also determine the allowed combination of SQUID-readout noise (S_ϕ) and multiplexer row-period (t_{row}) and row-count (N_{rows}). Recent improvements to S_ϕ and t_{row} in the NIST time-division-multiplexing architecture have allowed a NIST eight-pixel TES array to be read out with 2.70 eV (full-width at half-maximum) average energy resolution at 6 keV. The improvements make the X-ray Microcalorimeter Spectrometer co-proposed by NASA and NIST for ESA's Athena X-ray observatory straightforwardly achievable, including engineering margin, with $N_{rows} = 16$.

Keywords SQUID multiplexer · Transition-edge sensor · X-ray microcalorimeter

1 Introduction

One instrument envisioned for ESA's Athena X-ray mission is the X-ray Microcalorimeter Spectrometer (XMS), a 32×32 array of close-packed $250 \mu\text{m}$ -square transition-edge-sensor (TES) microcalorimeters covering a total field of view of 2.4×2.4

W.B. Doriese (✉) · B.K. Alpert · J.W. Fowler · G.C. Hilton · A.S. Hojem · K.D. Irwin ·
C.D. Reintsema · D.R. Schmidt · G.M. Stiehl · D.S. Swetz · J.N. Ullom · L.R. Vale
National Institute of Standards and Technology, Boulder, CO 80305, USA
e-mail: doriese@boulder.nist.gov

arcminute. With a per-pixel input X-ray count rate of $n = 50$ Hz, each XMS pixel is specified to produce an output count rate of $r \geq 40$ Hz with energy resolution of $\Delta E_{\text{FWHM}} \leq 3.0$ eV for $E_\gamma \leq 6$ keV and multiplexing factor of $N_{\text{rows}} = 16$.

A version of the XMS instrument is being proposed by the U.S. consortium of NASA/GSFC (MoAu TES arrays with “mushroom”-style absorbers) and NIST-Boulder (either time-division or code-division SQUID multiplexed readout, which are being developed in parallel). In 2008 this consortium demonstrated [1] time-division-multiplexed (TDM) readout of a close-packed array of 32 high-resolution NASA TES devices in various TDM configurations, with the key result that a 2-column \times 8-row array achieved $\langle \Delta E_{\text{FWHM}} \rangle = 2.93$ eV. The detectors, whose response and performance were very uniform, had critically damped time-constants of $\tau_{\text{crit}} = 280$ μs , and were similar in design to those proposed here for Athena.

In this paper, we optimize Athena’s detector-bias circuit. We show how ΔE_{FWHM} depends on $S_{I_{\text{MUX}}}$ (the detector-current-referred, multiplexed, SQUID-amplifier noise) and on t_{rec} , the length of the digitized records. We calculate Athena’s engineering margins for various combinations of SQUID noise and speed. Finally, we demonstrate recent improvements to the NIST TDM architecture.

2 Detector Model

Although Athena-XMS specifies $\Delta E_{\text{FWHM}} \leq 3.0$ eV, we specify here that after degradation due only to the multiplexed readout ($S_{I_{\text{MUX}}} \neq 0$ and $t_{\text{rec}} < \infty$), $\Delta E_{\text{FWHM}} \leq 2.7$ eV. This leaves engineering margin for other potential sources of degradation, such as imperfect gain-drift correction, electrical and thermal crosstalk among pixels, and nonuniformity in pixel bias.

The following linear detector model is based on TESs presently under production by NASA [2]. We follow the parameter usage of Irwin and Hilton [3]:

- $T_b = 50$ mK; $T_c = 90$ mK (cryogenic-bath and TES-critical temperatures)
- $C = 0.80$ pJ/K (TES heat capacity)
- $n = 3$ (thermal-conductivity index; unitless)
- $\alpha_I = 75$ (TES transition steepness; unitless)
- $R_0 = 1.0$ m Ω (TES quiescent resistance)
- $T_{\text{sh}} = 70$ mK (temperature of TES shunt resistor)
- $\beta_I = 1.25$ at $G = 200$ pW/K, and $\beta_I \propto G^{1/3}$

We allow the following TES-bias-circuit parameters to vary within practical ranges:

- G in the range 150 pW/K to 500 pW/K (thermal conductance to bath)
- R_{sh} in the range 50 $\mu\Omega$ to 1050 $\mu\Omega$ (TES shunt resistance)

and then derive others from them so as to have a self-consistent model:

- $k = G/(nT_c^{n-1})$ (thermal-conductivity coefficient)
- $P_{J_0} = k(T_c^n - T_b^n)$ (TES quiescent bias power, pW)
- $I_0 = \sqrt{P_{J_0}/R_0}$ (TES quiescent current, μA)
- L_{crit} (calculated inductance for critical damping [3], nH)

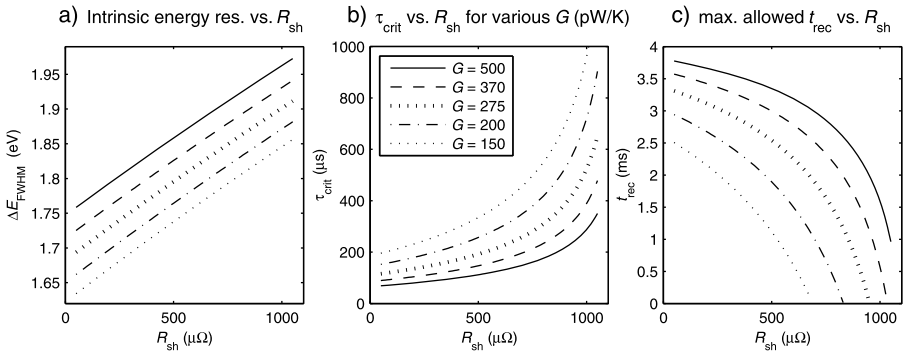


Fig. 1 (a) Energy resolution of the modeled detector, without readout degradation, as a function of G and R_{sh} . Resolution degrades with higher R_{sh} due to the increased contribution of the shunt’s Johnson noise. The dependence of β_I on G causes the dependence of resolution on G . For all choices of R_{sh} and G , this detector model provides significant margin in energy resolution below the limit of 2.7 eV. (b) The critically damped time-constant as a function of G and R_{sh} . (c) The maximum allowed record length to avoid too much pileup, determined by τ_{crit} and the count-rate specification, as a function of G and R_{sh}

The TES model above predicts [3, 4] energy resolution, based on linear response and Gaussian, stationary noise sources:

$$\frac{\Delta E_{FWHM}(G, R_{sh})}{\sqrt{8 \ln 2}} = \left(\int_{\frac{1}{2t_{rec}}}^{\infty} \frac{4|s_I(f)|^2 df}{S_{I_{TFN}}(f) + S_{I_{TES}}(f) + S_{I_{sh}}(f) + S_{I_{MUX}}(f)} \right)^{-\frac{1}{2}} \tag{1}$$

Here, $s_I(f)$ is the power-to-current responsivity of the TES (and is also the Fourier transform of a current pulse divided by its photon energy). The various S_I terms are, referred to the TES current: the thermal-fluctuation (phonon), TES-Johnson, shunt-resistor Johnson, and multiplexed amplifier (SQUID) noise spectra, and have units of A^2/Hz . Figure 1(a) shows the nondegraded ($S_{I_{MUX}} = 0$ and $t_{rec} \rightarrow \infty$) energy resolution in our linear-detector model as a function of R_{sh} for five values of G chosen to span the selected range.

Figure 1(b) shows τ_{crit} as a function of R_{sh} and G . Changes in G mainly affect the TES’s natural time-constant ($\tau_{nat} = C/G$), while changes in R_{sh} mainly affect electrothermal feedback (ETF).

3 Count Rate, Record Length, and Effective Bandwidth

In the standard Fourier-domain optimal filtering algorithm for microcalorimeter pulses [5], the time stream of data representing the detector current is digitized into records of fixed length, t_{rec} . An output record is allowed to contain only one current pulse. Via Poisson statistics, the Athena count-rate specification is thus: $r = n \exp[-n(t_{rec} + t_{RTB})] \geq 40$ Hz, where $n = 50$ Hz. The next event cannot come within t_{rec} after a no-pileup trigger, and the previous event cannot have occurred within the “return-to-baseline” time, t_{RTB} , before a no-pileup trigger. The Athena requirements yield $t_{rec} + t_{RTB} \leq 4.46$ ms.

The choice of t_{RTB} is somewhat arbitrary. We choose $t_{RTB} = 10\tau_{crit}$, so a critically damped current-pulse will have decayed to 0.1% of its peak current before another one may arrive and be considered a no-pileup event. This yields $t_{rec} \leq 4.46 \text{ ms} - 10\tau_{crit}$ to achieve the Athena count-rate specification; Fig. 1(c) shows the maximum allowed t_{rec} vs. G and R_{sh} .

Our recent study [4] discussed how t_{rec} affected ΔE_{FWHM} via the loss of the $f = 0$ bin in optimal filtering. We showed that τ_{crit} was a poor predictor of the t_{rec} required to achieve a given ΔE_{FWHM} ; instead, it was the effective bandwidth of the detector’s signal-to-noise-ratio density that was important. The effect of finite t_{rec} is included via the lower limit of integration in (1), $f = 1/(2t_{rec})$. If t_{rec} is too short, ΔE_{FWHM} can be substantially degraded.

4 SQUID Noise and Slew Rate: Dynamic-Slew Density

In either TDM or code-division-multiplexed (CDM) readout, the multiplexed SQUID noise is white. We find $S_{I,MUX}$ such that $\Delta E_{FWHM} = 2.7 \text{ eV}$, as determined by (1). This highest-allowed TES-referred SQUID noise is plotted in Fig. 2(a) vs. G and R_{sh} .

Figure 2(b) shows the maximum TES-current slew-rate, $I_{SR,max}$ (which occurs just after the photon arrival), for a 6 keV X-ray. The ratio, which we term the “dynamic-slew density,” of this maximum slew rate to the maximum tolerable multiplexed SQUID noise is the key metric of how big a burden the Athena specifications place on a CDM or TDM system for each detector model (see Fig. 2(c)). The lowest- G models, $G = 150 \text{ pW/K}$ (at its optimal $R_{sh} = 175 \mu\Omega$) and $G = 200 \text{ pW/K}$ (at $R_{sh} = 400 \mu\Omega$), are easiest to multiplex.

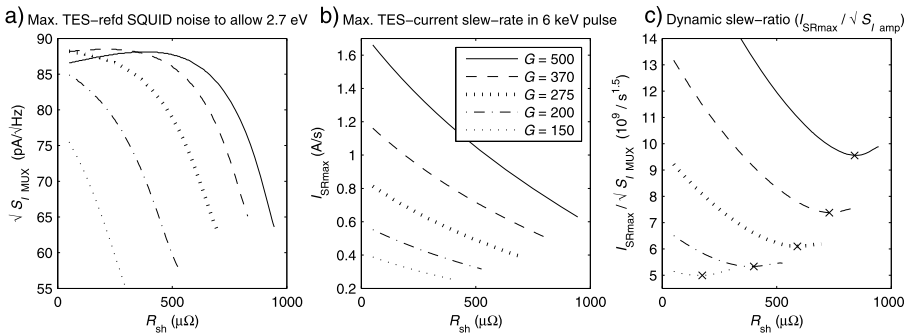


Fig. 2 (a) The maximum TES-referred SQUID noise that will allow $\Delta E_{FWHM} = 2.7 \text{ eV}$, as a function of G and R_{sh} . The degradation of ΔE_{FWHM} due to finite t_{rec} is included. (b) The maximum current-slew rate due to a 6 keV X-ray, as a function of G and R_{sh} . (c) The “dynamic-slew density” ((b) divided by (a)) required by the detector to achieve Athena’s specifications for 6 keV X-rays, as a function of G and R_{sh} . The y-units are physically not meaningful, but do allow relative comparisons among models. The ‘x’ shows the value of R_{sh} that minimizes this ratio for each value of G , and thus that places the lowest burden on the multiplexed readout. When multiplied by the multiplexing frame time (defined by the row-dwell time and the number of multiplexed rows, or $t_{fr} = t_{row}N_{rows}$) the dynamic-slew density is the “dynamic-range density” (units of $\sqrt{\text{Hz}}$) used [6] in discussion of frequency-domain multiplexing techniques

While the five models differ in G , and thus in τ_{nat} , by more than a factor of three, their optimal values of τ_{crit} range only from 200 μs to 235 μs . In addition to being easiest to multiplex in general, the higher-ETF models (low- G , low- R_{sh}) have two further advantages: (1) they suffer less thermal crosstalk; and (2) more of their multiplexing degradation is due to finite t_{rec} , so when Athena’s count rates were low during observations of dim sources, t_{rec} could be extended to improve ΔE_{FWHM} substantially.

5 Time-Division and Code-Division Specifications

Because SQUIDs have periodic response to input flux, SQUID multiplexers (both TDM and CDM) are run as digitally interleaved flux-locked loops, in which a feedback signal is applied once per frame to each first-stage SQUID in order to keep the SQUID output-current linear with input flux. A NIST first-stage SQUID will remain roughly linear as long as a given row’s TES current causes no flux change of more than Φ_0/π between samples of that row. Each row is sampled once per frame. Thus:

$$\Delta\Phi_{\text{max}} = I_{\text{SRmax}}M_{\text{in}}N_{\text{rows}}t_{\text{row}} \leq \Phi_0/\pi, \tag{2}$$

where $M_{\text{in}1}$ is the first-stage-SQUID input mutual-inductance. This relation holds explicitly for TDM. It holds approximately for CDM, away from the limit of very high count rates, and could be modified by replacing π with a larger number to allow pileup of the leading edges of pulses among different detectors in a CDM column.

In TDM, the relation between the maximum allowed TES-current-referred multiplexed SQUID noise (see Fig. 2(a)) and the nonmultiplexed SQUID noise (S_ϕ , referred to the first-stage SQUID) is, including the TDM aliasing factor [7]:

$$M_{\text{in}}\sqrt{S_{\text{IMUX}}} \geq \sqrt{\pi N_{\text{rows}}S_\phi}. \tag{3}$$

We factor out M_{in} to combine (2) and (3) and find a restriction on the product of the row time and nonmultiplexed SQUID noise in a TDM system:

$$t_{\text{row}} \sqrt{S_\phi} \leq \frac{\Phi_0}{I_{\text{SRmax}}} \sqrt{\frac{S_{\text{IMUX}}}{\pi^3 N_{\text{rows}}^3}}. \tag{4}$$

Figure 3(a) illustrates this requirement for TDM with $N_{\text{rows}} = 16$ for the value of R_{sh} at each G that minimizes the dynamic-slew density. The region under each curve is the allowed parameter space: faster SQUID switching and lower SQUID noise make multiplexing easier.

For CDM, which has no $\sqrt{N_{\text{rows}}}$ aliasing degradation, the equivalent to (3) is [8]:

$$M_{\text{in}}\sqrt{S_{\text{IMUX}}} \geq \sqrt{\pi S_\phi}. \tag{5}$$

The CDM equivalent to (4), plotted in Fig. 3, is:

$$t_{\text{row}} \sqrt{S_\phi} \leq \frac{\Phi_0}{I_{\text{SRmax}}} \sqrt{\frac{S_{\text{IMUX}}}{\pi^3 N_{\text{rows}}^3}}. \tag{6}$$

Recently, NIST has improved its TDM architecture and has developed a CDM architecture that is almost as mature [9]. In each, the non-multiplexed SQUID noise,

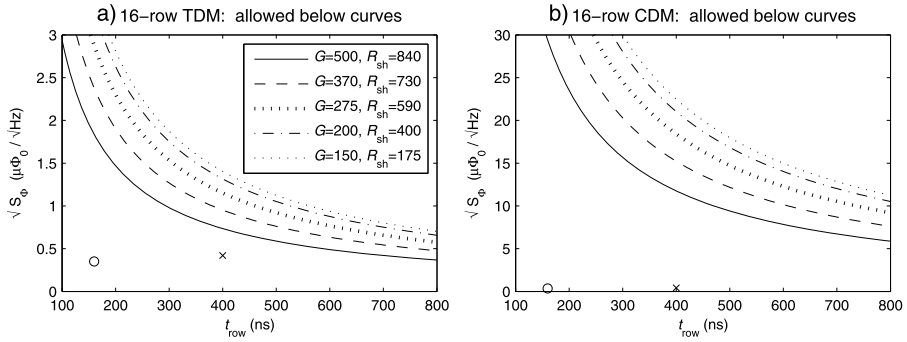


Fig. 3 Allowed combinations of SQUID noise and row time for the five modeled G (pW/K) values and their corresponding optimal values of R_{sh} ($\mu\Omega$) for 16-row (a) TDM and (b) CDM. The region under each curve satisfies Athena’s dual count-rate and energy-resolution requirements. ‘x’ in each plot marks the present state of the art for NIST multiplexers: 400 ns row-settle times and $\sqrt{S_\Phi} = 0.42 \mu\Phi_0/\sqrt{\text{Hz}}$. This condition provides engineering margin in SQUID noise of greater than 3 for TDM and more than 50 in CDM. ‘O’ marks our goal of 160 ns row times and $\sqrt{S_\Phi} = 0.35 \mu\Phi_0/\sqrt{\text{Hz}}$

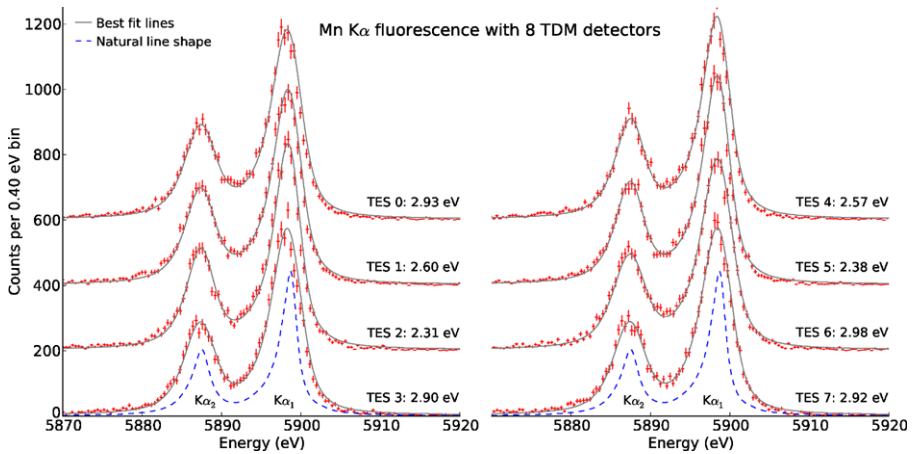


Fig. 4 (Color online) Energy spectra from eight NIST TESs read out through a single TDM column, with $\langle\Delta E_{FWHM}\rangle = 2.70$ eV. Detector time-constants ranged from 800 μs to 1600 μs because a range of inductance values was used. The analog row-settling time was 400 ns; the data link allowed t_{row} no faster than 640 ns, so the detectors were sampled for 240 ns of each row period

referred to the first-stage, is $\sqrt{S_\Phi} = 0.42 \mu\Phi_0/\sqrt{\text{Hz}}$, and the open-loop bandwidth allows a row-settling period of 400 ns. In the 2008 NIST/NASA TDM demonstration [1], these values were $\sqrt{S_\Phi} = 0.61 \mu\Phi_0/\sqrt{\text{Hz}}$ and 600 ns. The new parameters meet the Athena-XMS multiplexing requirements with appropriate engineering margin (Fig. 3). Figure 4 shows data from the improved TDM system. NIST TESs with much slower time constants than those of the proposed NASA Athena pixels were used because the Athena pixels were not yet available.

6 Conclusions

Present NIST SQUID-multiplexers, combined with NASA TES microcalorimeters, can instrument ESA's proposed Athena XMS package with significant engineering margin, as long as the detector bias circuit is optimized with a low- G , low- R_{sh} design. For 16 rows, TDM has more than a factor of three in noise margin, and CDM has so much margin that, were CDM deemed mature enough to be selected, Athena's mission specifications would likely be modified to take advantage.

Acknowledgements NIST and NASA/GSFC are jointly performing technology demonstrations for the Athena XMS instrument. We thank Caroline Kilbourne, Rich Kelley, Simon Bandler, Scott Porter, and the rest of the NASA group for useful discussions. Publication of an agency of the United States Government; not subject to copyright.

References

1. C.A. Kilbourne et al., SPIE Conf. Ser. **7011**, 701104 (2008)
2. N. Iyomoto et al., Appl. Phys. Lett. **92**, 013508 (2007)
3. K.D. Irwin, G.C. Hilton, in *Cryogenic Particle Detection*, ed. by C. Enss (Springer, Berlin, 2005)
4. W.B. Doriese et al., AIP Conf. Proc. **1185**, 450–453 (2009)
5. A.E. Szymkowiak et al., J. Low Temp. Phys. **93**, 281–285 (1993)
6. R.H. den Hartog et al., IEEE Trans. Appl. Supercond. **21**(3), 289–293 (2011)
7. W.B. Doriese et al., Nucl. Instrum. Methods Phys. Res., Ser. A **559**, 808–810 (2006)
8. K.D. Irwin et al., Supercond. Sci. Technol. **23**, 034004 (2010)
9. J.W. Fowler et al., J. Low Temp. Phys. (2012). doi:[10.1007/s10909-012-0463-4](https://doi.org/10.1007/s10909-012-0463-4)